an alpha-step surface profilameter indicates that variations in surface roughness typically range from 100 to 500 Å over a scan length of 1 mm. Variations as large as a few thousand angstroms can be spotted occasionally. These preliminary results are very encouraging for potential superconducting device applications. It is hoped that in the future, thinner and optimized films will have even better surface morphology.

The synthesis of high-quality Hg-cuprate films has posed one of the toughest challenges so far in the area of high T_c films because of the highly volatile nature of Hg-based compounds. Various standard thin-film techniques for volatile materials failed to achieve high-quality Hg-cuprate films. Only after the adoption of multitarget atomic-scale mixing, cap layers, and controlled annealing techniques were such films achieved reproducibly. The atomic-scale mixing and the protective cap layer ensure stoichiometric composition before annealing. The as-deposited films prepared by Wang *et al.* (4) contained no Hg at all and required diffusion of Hg into the film after deposition. This procedure is likely to be more prone to film inhomogeneity, especially degradation at the grain boundaries, which may account for the lack of electrical connectivity in their films. In addition, given the high volatility of Hg compounds, the use of a single stoichiometric target (which was also tried) leads to insulating films, almost certainly because of preferential deposition.

Our approach provides for a precise control of the Hg content in the film, which is key to success. In a more general sense, the technique presented in this work is expected to find more general applications in the synthesis of thin films containing volatile materials other than mercury. In view of their excellent electrical and magnetic characteristic, these films are expected to be useful in applications of Josephson junctions such as grain boundary SQUIDs and other devices.

REFERENCES AND NOTES

1. S. N. Putilin, E. V. Antipov, O. Chmaissem, M. Marezio, *Nature* **362**, 226 (1993).
2. A. Schilling, M. Cantoni, J. D. Guo, H. R. Ott, *ibid.* **363**, 56 (1993).
3. C. W. Chu *et al.*, *ibid.* **365**, 323 (1993).
4. Y. Q. Wang *et al.*, *Appl. Phys. Lett.* **63**, 3084 (1993).
5. W. Y. Lee *et al.*, *ibid.* **60**, 772 (1992).
6. C. A. Neugebauer, in *Handbook of Thin Film Technology*, L. I. Maissel and R. Glang, Eds. (McGraw Hill, New York, 1970), pp. 8–22.
7. P. A. Saunders and J. F. Ziegler, *Nucl. Instrum. Methods Phys. Res.* **218**, 67 (1983).
8. R. L. Meng *et al.*, *Phys. C* **216**, 21 (1993).
9. We thank G. Coleman, C. Feild, P. Duncombe, and E. Kummer for their technical assistance and A. Guloy, C. C. Chi, B. Mercey, M. Ketchen, and B. A. Scott for helpful discussions. Supported in part by the Defense Advanced Research Projects Agency under contract N00014-89-0112.

9 December 1993; accepted 6 January 1994

Atomic Force Microscopy of the Electrochemical Nucleation and Growth of Molecular Crystals

Andrew C. Hillier and Michael D. Ward*

In situ atomic force microscopy reveals the morphology, surface topography, and growth and dissolution characteristics of microscopic single crystals of the low-dimensional organic conductor (tetrathiafulvalene)$Br_{0.76}$, which are grown by electrocrystallization on a highly oriented pyrolytic graphite electrode in an atomic force microscope liquid cell. The growth modes and the distribution and orientation of topographic features on specific crystal faces, whose identity was determined by "atomic force microscope goniometry," can be correlated with the strength and direction of anisotropic solid-state intermolecular bonding. Growth on the (011) face of (tetrathiafulvalene)$Br_{0.76}$ crystals involves the formation of oriented self-similar triangular islands ranging in size from 200 to 5000 angstroms along a side. These nuclei eventually transform into rectangular rafts at larger length scales, where bulk intermolecular bonding interactions and surface energies dominate over nuclei-substrate interactions.

Molecular crystals containing organic components exhibit a variety of electronic properties, including electrical conductivity, superconductivity, nonlinear optical behavior, and ferromagnetism (*1*), and also comprise the majority of pharmaceutical reagents (*2*). Much of the interest in these materials stems from the ability to use molecular-level "crystal engineering" strategies (*3*) to control solid-state intermolecular interactions in order to rationally manipulate crystal packing and, consequently, influence bulk physical and electronic properties. Although these strategies have been used in the design and synthesis of many organic crystals, the self-assembly, nucleation, and crystallization processes that are responsible for their formation are not well understood, particularly at the molecular level and nanometer length scales. This understanding is crucial if important crystal characteristics such as polymorphism, morphology, inclusion formation, and defect density are to be controlled.

Recent developments in atomic force microscopy (AFM) (*4*), however, now provide for in situ visualization of the early stages of growth of organic crystals in liquids (*5–7*). This capability allows dynamic observation of nucleation events and the determination, at small length scales, of the distribution of topographic features (that is, terraces, ledges, and kinks) that play an important role in crystal growth (*8*). We made in situ AFM observations of the electrochemical nucleation and growth of the crystalline quasi–one-dimensional organic conductor (TTF)$Br_{0.76}$ (TTF, tetrathiafulvalene) (*9*), wherein the rate of crystal growth was regulated by the electrochemical potential applied during the electrocrystallization process (*10*). Electrocrystallization is a convenient method for AFM visualization of crystal growth modes because the supersaturation at the crystal surface can be controlled by the electrochemical potential, analogous to the effect of changing solute concentration during the growth of nonconducting crystals. We chose (TTF)$Br_{0.76}$ because it is representative of low-dimensional organic conductors and previous studies (*11*) indicated that growth occurred readily on existing nuclei during electrocrystallization.

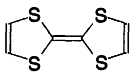

TTF

Electrochemical nucleation and growth of well-defined needle crystals of the conductive, nonstoichiometric salt (TTF)$Br_{0.76}$ on a freshly cleaved, highly oriented pyrolytic graphite (HOPG) electrode was accomplished readily in an AFM liquid cell (*12*). Crystallization was induced by the brief application (1 to 5 s) of an anodic potential step in the range $0.40 \leq E_{applied} \leq 0.70$ V [versus a saturated calomel electrode (SCE)] (*13*). Under these conditions, AFM revealed nucleation of (TTF)$Br_{0.76}$ crystals on the HOPG electrode, with nucleation densities approaching 10^3 mm^{-2}. These needle crystals exhibited widths ranging from 0.2 to 4 μm, lengths of 10 to 15 μm, and heights of 0.1 to 0.75 μm. The needle axis of the

---

Department of Chemical Engineering and Materials Science, University of Minnesota, Amundson Hall, 421 Washington Avenue, S.E., Minneapolis, MN 55455, USA.

*To whom correspondence should be addressed.

crystals was always parallel to the HOPG substrate, but no azimuthal orientation was observed (*14*). Subsequent growth or dissolution of these crystals could be precisely controlled by selection of the applied electrochemical potential.

$$\mathrm{TTF} + 0.76\ \mathrm{Br}^- \rightarrow (\mathrm{TTF})\mathrm{Br}_{0.76} + 0.76e^- \qquad (1)$$

The microscopic $(\mathrm{TTF})\mathrm{Br}_{0.76}$ crystals exhibited several distinct faces, each with a unique morphology and topography (Fig. 1). The most prominent face was parallel to the substrate and extended along the needle axis of the crystal. This plane was identified as (010) by comparison of high-resolution AFM data to the molecular packing of this plane (*15*). The periodicity of contrast was 15.01 and 3.25 Å along [100] and [001], respectively, in good agreement with the x-ray structure values of 15.617 and 3.572 Å. Molecular resolution on the other faces proved difficult because of the highly stepped nature of these faces (*16*). However, the remaining faces could be assigned by "AFM goniometry," in which the dihedral angles between the faces were measured from AFM height data (*17*). A self-consistent set for the observed planes includes (010), $(\bar{3}10)$, and (210), which are parallel to [001], and (011) appearing on the crystal apex (*18, 19*). The $(\bar{3}11)$ and (211) planes were also occasionally observed at the tip of the crystal (*20*).

The closely packed (010) face exhibits [001] ledges with step heights of 6.3 to 7.2 Å, in good agreement with the TTF layer spacing normal to the (010) plane (Fig. 2). The [001] ledges are enforced by strong intermolecular bonding energies ($\phi_{[001]}$) (*21*) along the [001] stacking axis associated with π-π charge transfer interactions between TTF molecules. The average width of the (010) terraces exceeded 3000 Å, reflecting a large $\phi_{[100]}$, which can be attributed to strong electrostatic interactions between stacks of TTF^+ cations and the Br^- counterions along [100]. The presence of two strong in-plane bonding interactions in (010) provides for a low surface energy, $\gamma_{(010)}$, resulting in large (010) faces in macroscopic crystals (*8, 22*). In addition, real-time imaging of growth on the (010) face indicated a two-dimensional nucleation and growth mode, consistent with two strong bonding vectors in this plane.

In contrast to (010), AFM data indicate that the $(\bar{3}10)$ face has a high density of [001] ledges with step heights of 15 or 21 Å, equivalent to two or three TTF layers, respectively. The average width of these ledges is <25 Å. The $(\bar{3}10)$ face is therefore best described as a high energy, highly stepped, vicinal face containing (010) terraces and (100) steps of molecular dimensions. The mode of crystal growth on $(\bar{3}10)$ differs considerably from that observed on (010), occurring by the relatively rapid advancement of kinks along the [001] ledges, consistent with favorable intermolecular bonding ($\phi_{[001]}$) along this direction. These kinks are evident as features parallel to

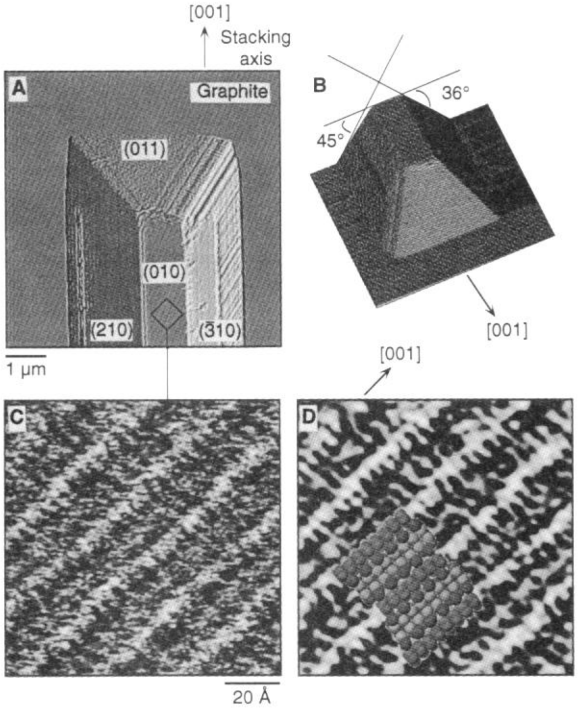

Fig. 1. AFM images of a $(\mathrm{TTF})\mathrm{Br}_{0.76}$ crystal growing on a HOPG electrode with [001] parallel to the basal plane of graphite. (**A**) Image of a crystal and the assigned planes. (**B**) Surface plot of the AFM height data illustrating the crystal geometry (crystal height corresponds to 7500 Å). (**C**) An image of the (010) face showing molecular resolution (raw data). (**D**) An image of the (010) face after Fourier filtering. The molecular packing of (010) is superimposed on (D).

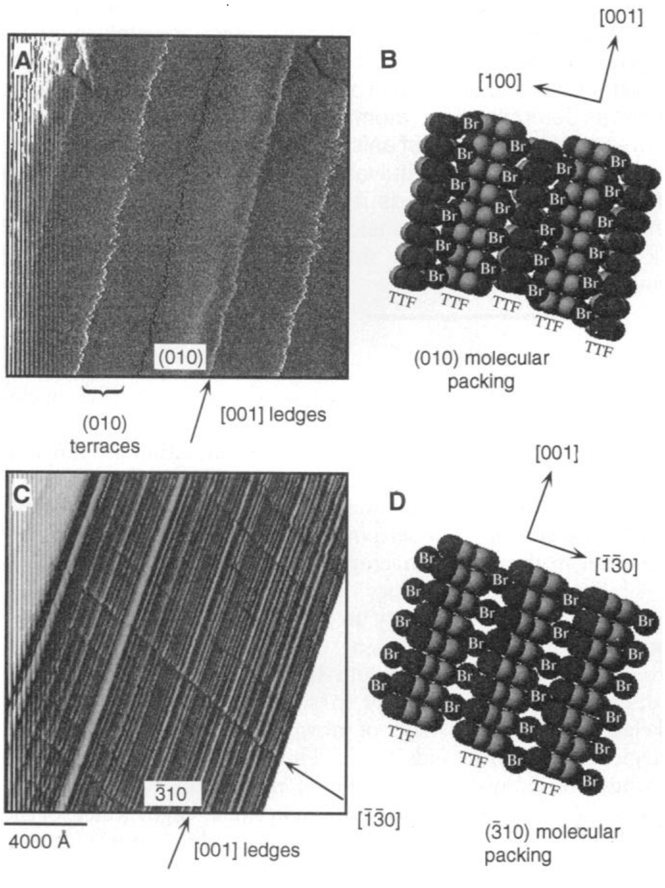

Fig. 2. Nanoscopic surface morphology exhibited by exposed faces of $(\mathrm{TTF})\mathrm{Br}_{0.76}$ during growth on HOPG. (**A**) Surface structure and (**B**) molecular packing of the (010) face. The AFM image consists of [001] ledges formed from large, molecularly smooth (010) terraces intersected by steps with heights of 6.3 to 7.2 Å. (**C**) Surface structure and (**D**) molecular packing of the $(\bar{3}10)$ face. The AFM image reflects a high ledge density on $(\bar{3}10)$ with ledges along [001] and kinks along $[\bar{1}\bar{3}0]$. The step heights of the ledges are 15 to 21 Å, corresponding to two or three TTF layers. The TTF cation stacks and Br^- anions are shown in (B) and (D), but the TTF hydrogen atoms have been omitted for clarity. The vertical striations on the extreme left of the AFM images are caused by cantilever oscillation resulting from high feedback.

$[\bar{1}\bar{3}0]$. This process leads to accumulation on the [001] ledges and, consequently, their advancement along [100]. The $(\bar{3}10)$ face grows out of existence at larger length scales by bunching of the ledges, which thereby generates the large (010) terraces. These results indicate that the surface topography and growth modes observed on $(TTF)Br_{0.76}$ crystals can be rationalized on the basis of solid-state intermolecular bonding interactions that exist within the plane of each distinct crystal face. The slow two-dimensional growth observed on (010) and the ledge bunching on $(\bar{3}10)$ conspire to give the (010) face a large morphological importance in the macroscopic crystal.

Crystal planes exposed on the tip of a $(TTF)Br_{0.76}$ crystal, however, do not contain the [001] stacking axis. As a result, these faces tend to be microscopically rough, and the corresponding growth mechanism does not appear to involve clearly defined ledges. The (011) face, which is the predominant face exposed on the tip of a $(TTF)Br_{0.76}$ crystal, exhibits a pyramidal habit, intersecting the $(\bar{3}10)$ and (210) planes along the $[13\bar{3}]$ and $[\bar{1}2\bar{2}]$ zones (Fig. 1A). Notably, nucleation on (011) occurs with the formation of oriented triangular nuclei (Fig. 3). One edge of the triangles is oriented at angle of 23° with respect to $[13\bar{3}]$. Initially, these triangular features exhibit dimensions of 200 Å on a side (area ≈ 9000 Å^2) and 50 Å in height, evolving over time to 5000 Å on a side and 300 Å in height.

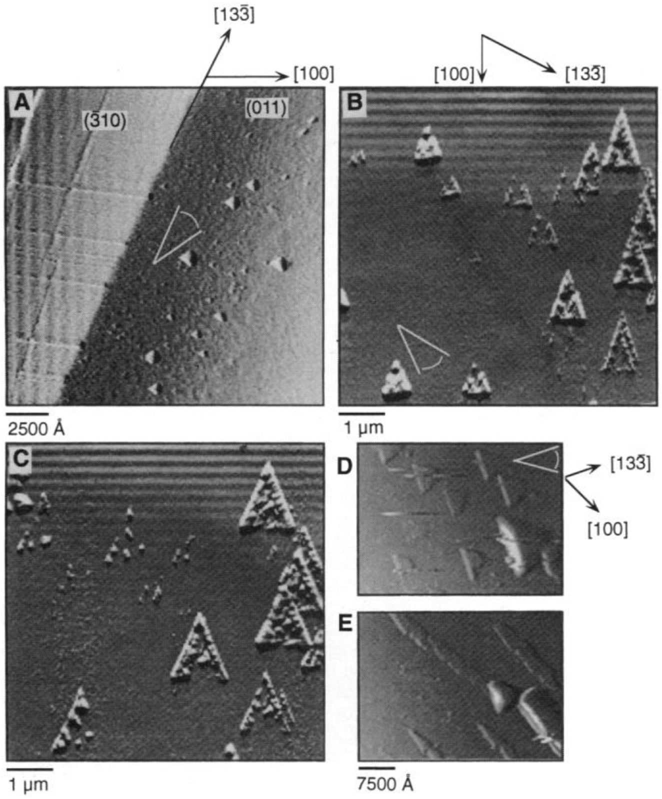

Fig. 3. Images of triangular islands appearing on the (011) face of $(TTF)Br_{0.76}$ during growth. (**A**) AFM image of oriented triangular islands on (011). Also indicated is the $[13\bar{3}]$ zone axis that lies along the intersection of the (011) and $(\bar{3}10)$ planes. (**B**) Aggregation of the triangular nuclei on (011). The angle between the $[13\bar{3}]$ direction and the edge of the triangles (indicated in white) was experimentally measured to be 23° ± 5°. (**C**) The same region as in (B) after 60 s (several islands exhibit a Sierpinski gasket self-similarity). Images of the triangular nuclei (**D**) before and (**E**) after their transformation to the rectangular raft morphology. The images in (A), (B) and (C), and (D) and (E) were obtained on different crystals in separate experiments.

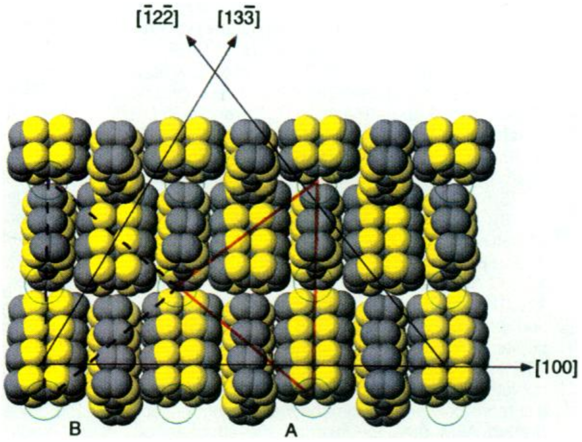

Fig. 4. Molecular packing of the (011) face of $(TTF)Br_{0.76}$. The intersection of the (011) face with the $(\bar{3}10)$ and (210) faces is defined by the $[13\bar{3}]$ and $[\bar{1}2\bar{2}]$ zone axes, respectively. The molecular kink sites on (011) are indicated by the open circles. The orientation and shape of the triangular nuclei (Fig. 3) are identical to the triangle constructed here from the kink sites defined by the solid lines (denoted as A). The angle subtended by the $[13\bar{3}]$ zone axis and the upper edge of the triangle is 23°. The orientation that would result from the triangular array of kinks defined by the dashed lines (denoted as B) is not observed. Because of the monoclinic symmetry of $(TTF)Br_{0.76}$, orientations A and B are not crystallographically equivalent. The TTF hydrogen atoms and the Br^- anions have been omitted for clarity.

These nuclei exhibit remarkable self-similarity over this entire size range, maintaining their orientation and aspect ratio. Indeed, the larger triangles are frequently observed as aggregates of smaller ones of the same orientation; consequently, they exhibit a "fractal" structure, resembling disordered Sierpinski gaskets (Fig. 3, B and C) (*23*). The size distribution of the smaller triangles that make up the gaskets appears to be fairly uniform, in contrast to true ordered Sierpinski gaskets, which are constructed from a generator that results in an ensemble of self-similar triangles of different sizes. Under the conditions where these gaskets are observed, the aggregation of the smaller triangles may occur either by diffusion along the (011) surface until attachment to other nuclei or, more likely, by a nucleation-redissolution mechanism in which small triangular nuclei persist upon aggregation with others.

The (011) plane of $(TTF)Br_{0.76}$ is best described as a highly stepped, vicinal plane consisting of [100] oriented ledges formed by monomolecular (001) step planes and (010) terraces (Fig. 4). Furthermore, the [100] ledges contain molecular kink sites that are a consequence of the alternating orientation of the TTF molecules along this direction. Notably, a triangular array of these kinks can be constructed (denoted A in Fig. 4) whose orientation is identical to that of the triangular nuclei on the (011) face. This strongly supports a mechanism in which the observed nucleation behavior involves preferential attachment of incoming solute molecules to these kink sites and fast aggregation between these sites along directions corresponding to the edges of the triangles. While it may seem surprising that an opposite orientation is not observed (denoted B in Fig. 4), the two orientations are crystallographically unique under the symmetry of the monoclinic space group. Apparently, the chemical inequivalence resulting from the crystallographic inequivalence is sufficient to provide discrimination between the two orientations.

The triangular features observed during early stages of growth eventually evolve into oriented rectangular rafts whose long axis is parallel to [100] (Fig. 3, D and E). This evolution suggests that the formation of the triangular nuclei results from a kinetic preference for the quasi threefold

(011) kink sites, whereas at larger length scales, factors such as bulk thermodynamic bonding and surface energy supersede these interactions. The dominant intermolecular bonding within the (011) face is the electrostatic interaction along [100], which enforces the [100] ledge structure. The observed morphology after this transformation is indicative of the strong electrostatic $\phi_{[100]}$ bonding in the bulk and the more favorable surface energy of planes associated with the growth along [100], which overrides the substrate-nuclei interactions as the nuclei become larger. Indeed, the crystal faces exposed on the sides of the triangular nuclei will have substantial surface energy attributable to their roughness.

Our results clearly indicate that the surface topography and crystal growth modes depend on the crystal face, generally reflecting the strength of intermolecular solid-state bonding within the crystallographic planes defining those faces. However, it is evident that the molecular-level topography, such as that of the (011) face of (TTF)Br$_{0.76}$, can strongly influence morphology in the early stages of nucleation where substrate-nuclei interactions can predominate over bulk bonding enthalpies and surface energies that become important at large length scales. Further examination of nucleation and growth at the nanometer length scale will likely lead to other unanticipated length scale–dependent behaviors, while providing an opportunity to unravel the fundamental principles that control crystal growth at the molecular level.

REFERENCES AND NOTES

1. J. S. Miller, A. J. Epstein, W. M. Reiff, *Science* **240**, 40 (1988); J. S. Miller, *Extended Linear Chain Compounds* (Plenum, New York, 1982), vols. 1–3; A. F. Garito and A. J. Heeger, *Acc. Chem. Res.* **7**, 232 (1974); J. B. Torrance, *ibid.* **12**, 79 (1979); J. Zyss and G. Tsoucaris, in *Structure and Properties of Molecular Crystals*, M. Pierrot, Ed. (Elsevier, Amsterdam, Netherlands, 1990), pp. 297–350.
2. S. R. Byrn, *Solid-State Chemistry of Drugs* (Academic Press, New York, 1982).
3. G. M. J. Schmidt, *Pure Appl. Chem.* **27**, 647 (1971); G. Desiraju, *Crystal Engineering—The Design of Organic Solids* (Elsevier, New York, 1989); J. M. Lehn, *Angew. Chem. Int. Ed. Engl.* **27**, 89 (1988); P. J. Fagan, M. D. Ward, J. C. Calabrese, *J. Am. Chem. Soc.* **111**, 1698 (1989).
4. G. Binnig, C. F. Quate, Ch. Gerber, *Phys. Rev. Lett.* **12**, 930 (1986); G. Binnig, Ch. Gerber, E. Stoll, T. R. Albrecht, C. F. Quate, *Europhys. Lett.* **3**, 1281 (1987).
5. A. J. Gratz, S. Manne, P. K. Hansma, *Science* **251**, 1343 (1991); P. E. Hillner, S. Manne, A. J. Gratz, P. K. Hansma, *Ultramicroscopy* **42–44**, 1387 (1992); P. E. Hillner, A. J. Gratz, S. Manne, P. K. Hansma, *Geology* **20**, 359 (1992); S. D. Durbin and W. E. Carlson, *J. Cryst. Growth* **122**, 71 (1992); S. J. Manne, J. P. Cleveland, G D. Stucky, P. K. Hansma, *ibid.* **130**, 333 (1993).
6. B. Drake *et al.*, *Science* **243**, 1586 (1989); O. Marti, B. Drake, P. K. Hansma, *Appl. Phys. Lett.* **51**, 17 (1987); S. Manne, H. J. Butt, A C. Gould, P K. Hansma, *ibid.* **56**, 1758 (1990); S. Manne, J. Massie, V. B. Elings, P. K. Hansma, A. A. Gewirth, *J. Vac. Sci. Technol. B* **9**, 950 (1991); C. Chen and A. A. Gewirth, *Ultramicroscopy* **42–44**, 437 (1992).
7. F. Ohnesorge and G. Binnig, *Science* **260**, 1451 (1993); A. L. Weisenhorn, P. K. Hansma, T. R. Albrecht, C. F. Quate, *Appl. Phys. Lett.* **54**, 2651 (1989); J. L. Hutter and J. Bechhoefer, *J. Appl. Phys.* **73**, 4123 (1993).
8. P. W. Carter, A. C. Hillier, M. D. Ward, *J. Am. Chem. Soc.*, in press.
9. F. B. Kaufman, E. M. Engler, D. C. Green, J. Q. Chambers, *ibid.* **98**, 1596 (1976); P. Kathirgamanathan and D. R. Rosseinsky, *Chem. Commun.* **1980**, 356 (1980); P. A. C. Gane, P. Kathirgamanathan, D. R. Rosseinsky, *ibid.* **1981**, 378 (1981); M. Lamache and K. E. Kacemi, *Mol. Cryst. Liq. Cryst.* **120**, 255 (1985); J. B. Torrance and B. D. Silverman, *Phys. Rev. B* **15**, 788 (1977). The true composition of the conductive (TTF)Br$_x$ salt ranges from $0.72 < x < 0.80$. The composition defines the extent of oxidation of the TTF chains, with the anions serving to neutralize charge. The value of $x = 0.76$ was chosen because it is the average composition of the mixed-valent (TTF)Br$_x$ salt.
10. M. D. Ward, *Electroanalytical Chemistry* (Dekker, New York, 1990), and references therein.
11. ———, *J. Electroanal. Chem.* **135**, 2747 (1988).
12. The AFM experiments were performed with a Digital Instruments Nanoscope III scanning probe microscope equipped with a scan head having a maximal scan range of 125 μm by 125 μm by 5 μm and with Nanoprobe cantilevers (Si_3N_4 with integral tips having spring constants of 0.06 N m^{-1}). Images were obtained simultaneously in both constant-force and error modes with filters off, an integral gain of 3.0, a proportional gain of 7.0, and a look-ahead gain of 0.0. The error mode, equivalent to a height image that has been high-pass filtered, provided enhanced contrast. The AFM electrochemical cell (Digital Instruments) consisted of a freshly cleaved HOPG working electrode, a platinum counter electrode, and a silver quasi reference electrode. The HOPG electrode exhibited well-defined atomic structure and nanometer-scale flatness over length scales of tens of micrometers. The electrolyte solution consisted of 5 mM TTF (Aldrich) in a 0.1 M solution of n-$Bu_4N^+Br^-$ (Aldrich) in ethanol.
13. Standard reduction potentials for TTF: $E°$ (TTF-TTF$^+$) = 300 mV; $E°$ (TTF$^+$-TTF^{2+}) = 660 mV versus SCE.
14. The parallel crystal growth orientation is common in the AFM electrochemical fluid cell because of the restricted cell geometry. When an electrochemical cell that allows isotropic transport is used, growth of (TTF)Br$_{0.76}$ crystals generally occurs with a random azimuthal and colatitudinal orientation. The AFM fluid-cell geometry is thin, and the placement of the counter electrode results in enhanced migration parallel to the HOPG surface, which favors the observed lateral growth.
15. The single-crystal x-ray structure of (TTF)Br$_{0.76}$ reveals separate TTF and Br sublattices, which both pack in the monoclinic $C2/m$ space group [B. A. Scott, S. J. La Placa, J. B. Torrance, B. D. Silverman, B. Welber, *J. Am. Chem. Soc.* **99**, 6631 (1977); S. J. La Placa, P. W. R. Cornfield, R. Thomas, B. A. Scott, *Solid State Commun.* **17**, 635 (1975); G. Theodorou, *Phys. Rev. B* **19**, 1132 (1979)]. Lattice parameters for the $C2/m$ TTF sublattice: a = 15.617 Å, b = 15.627 Å, c = 3.572 Å, and β = 91.23°; for the $C2/m$ Br sublattice: a = 17.368 Å, b = 15.623 Å, c = 4.538 Å, and β = 116.01°. The sublattices have identical [010] lattice parameters, but the cell length of the Br sublattice along [001] is longer than that of the TTF sublattice, and the [100] directions of the sublattices subtend an angle of 24.8°. Therefore, it is more convenient from the standpoint of interpreting AFM data to describe the structure of (TTF)Br$_{0.76}$ by a supercell based on the isomorphic salt (TTF)I$_x$ (x = 5/7), whose structure has been solved according to the monoclinic $P2_1/a$ space group [J. J. Daly and F Sanz, *Acta Crystallogr. Sect. B* **31**, 620 (1975); C. K. Johnson and C. R. Watson, *J. Chem. Phys.* **64**, 2271 (1976)]. The (TTF)I$_{5/7}$ and (TTF)Br$_{5/7}$ supercells each incorporate the anion and cation sublattices into a single unit cell with a = 48.165 Å (46.851 Å), b = 16.052 Å (15.627 Å), c = 24.943 Å (25.004 Å), and β = 91.13° (91.23°). Lattice constants in parentheses refer to (TTF)Br$_{5/7}$.
16. Typical AFM scanning tips have a radius of curvature ranging from 200 to 2000 Å, as determined by scanning electron microscopy, so there is a finite interaction region between tip and sample. Meaningful molecular-scale information requires that the tip interacts with a surface that is molecularly smooth over an area that is considerably larger than the interaction area of tip and sample. Therefore, the AFM cannot obtain lateral molecular-level resolution on a surface with a high density of ledges. The height of these steps, however, can be accurately determined to within a fraction of an angstrom.
17. As a note of caution, the resolution that can be obtained when measuring a dihedral angle with the AFM depends on the aspect ratio of the cantilever tip. The maximum measurable angle between a terrace and a step [illegible] typical Si_3N_4 AFM tips with a 1:1 aspect ratio, whereas the maximum measurable angle with Si cantilevers with a 3:1 aspect ratio is 75°. For most of these experiments, Si_3N_4 cantilevers were used. However, when the observed angle approached 55°, we used a Si cantilever to verify the results.
18. Dihedral angles measured by AFM compared with those determined from the x-ray crystal structure (in parentheses) of the (TTF)I$_{5/7}$ supercell: (010) ∩ (210) = 36° (34°); (010) ∩ $(\bar{3}10)$ = 43° (45°); (010) ∩ (011) = 33° (33°); (210) ∩ (011) = 50° (45°); and $(\bar{3}10)$ ∩ (011) = 50° (54°). These dihedral angles, as measured with AFM, were independent of the azimuthal orientation of the (TTF)Br$_{0.76}$ crystals with respect to the AFM tip. This morphology was also corroborated by scanning electron microscopy of crystals of similar size. These observations rule out artifacts attributable to tip geometry in the measurements of the dihedral angles.
19. The structure of (TTF)Br$_{0.76}$ is monoclinic and, thus, exhibits crystallographically (and chemically) distinct (100) and (010) faces. However, the difference between these planes results from only a 1.23° (β = 91.23°) offset of the TTF molecules in the (010) plane, as compared with (100). This difference is too slight to be differentiated with the interfacial angles or the high-resolution molecular-level registry as determined by the AFM. Thus, an alternative assignment of the exposed faces of Fig. 1 would be (100), (310), and $(4\bar{1}0)$ along the [001] zone and (103) at the crystal tip. Use of these alternative assignments would not alter the interpretation of the nucleation and growth behavior.
20. A smooth face that was parallel to the [001] stacking axis and formed a small dihedral angle with (010) was occasionally observed. This face is attributed to twinning, as its morphology and surface topography appear to be a mirror image of the aforementioned (010) plane.
21. The intermolecular bonding energy $\phi_{[uvw]}$ is defined as the projection of the global solid-state bonding interaction Φ along the [uvw] direction.
22. P. Hartman and W. G. Perdok, *Acta Crystallogr.* **8**, 49 (1955); *ibid.*, p. 521; *ibid.*, p. 525.
23. B. B. Mandelbrot, *The Fractal Geometry of Nature* (Freeman, San Francisco, CA, 1979); D. Avnir, Ed., *The Fractal Approach to Heterogeneous Chemistry* (Wiley, Chichester, United Kingdom, 1989).

24. We acknowledge the support of the Office of Naval Research and the Center for Interfacial Engineering (NSF Engineering Research Centers Program). A.C.H. acknowledges the Upjohn Company for support in the form of an Upjohn Fellowship during 1992–1993.

5 November 1993; accepted 1 February 1994